Additive Manufacturing Letters 3 (2022) 100069

Contents lists available at ScienceDirect

Additive Manufacturing Letters

journal homepage: www.elsevier.com/locate/addlet

Effect of Y_2O_3 dispersoids on microstructure and creep properties of Hastelloy X processed by laser powder-bed fusion

Jovid U. Rakhmonov [a,*], Christoph Kenel [a], Anthony De Luca [b], Christian Leinenbach [b,c], David C. Dunand [a]

[a] Department of Materials Science & Engineering, Northwestern University, Evanston, IL, 60208-3108, USA
[b] Empa – Swiss Federal Laboratories for Materials Science and Technology, Überlandstrasse 129, 8600 Dübendorf, Switzerland
[c] École Polytechnique Fédérale de Lausanne (EPFL), Laboratory for Photonic Materials and Characterization, 1015 Lausanne, Switzerland

ARTICLE INFO

Keywords:
Hastelloy X
Laser powder bed fusion
Oxide dispersion strengthening
Texture
Creep

ABSTRACT

Laser powder bed fusion (LPBF) was used to consolidate powders of a Ni-Cr-Fe-Mo alloy (Hastelloy X) blended with 1 wt% Y_2O_3 nanometric powders. The nearly-dense, crack-free specimens, with and without oxide dispersion strengthening (ODS), exhibit high-aspect ratio grains, aligned in the build direction and with a strong texture: ⟨001⟩ is aligned along both build direction and laser scanning direction. Creep tests performed at 950 °C, with compressive stresses aligned with the elongated grains (and the build direction), reveal two creep regimes:

(i) at stresses below ~50 MPa, diffusional creep dominates, and the ODS alloy is less creep resistant than the non-ODS alloy, consistent with a somewhat smaller grain size resulting from grain-boundary pinning by the oxide dispersoids; (ii) at stresses above ~50 MPa, dislocation creep dominates and the ODS alloy is more creep resistant, as expected from oxide dispersoids impeding dislocation motion. When tested perpendicular to the build direction, both alloys have the same creep resistance, which is however much lower than when the stress is aligned with the build direction, reflecting a strong effect of texture and grain shape. After ~10% compressive creep deformation, grain structure and texture remain largely unchanged as compared to pre-creep structure.

1. Introduction

Hastelloy X (HX) is a nickel alloy displaying high levels of solid-solution strengthening at ambient and elevated temperature provided by the high concentrations of Cr (20–23%), Fe (17–20%) and Mo (8–10%), as well as minor amounts of Co (0.5–2.5%) and W (0.2–1%). The high Cr concentration also provides outstanding oxidation- and corrosion resistance [1]. Because it lacks the $L1_2$-γ' precipitates present in Ni-based superalloys, HX shows excellent cold- and hot-workability, weldability, and machinability, albeit without the very high creep resistance of γ'-strengthened superalloys. Oxide-dispersion strengthening - a widely used strategy to achieve improvements in creep resistance in various alloys [2,3] - has been implement in HX via mechanical alloying followed by powder densification [4], and more recently via the spray-dispersion method where oxide particles are injected in the metal stream during casting [5].

The additive manufacturing of HX has been extensively studied, with focus on microstructure [6,7], cracking prevention [8–11], alloying additions, ambient-temperature strength [8,12] and high-temperature deformation [13]. Much less research has been performed on ODS-HX fabricated by additive manufacturing methods. Cheng *et al.* [14] achieved additions of 1 wt.% Y_2O_3 in HX by laser powder bed fusion (LPDF) of HX powders coated with yttrium nitrate hydrate, which decomposed to the oxide during processing: the resulting 20 nm Y_2O_3 dispersoids reduced cracking propensity, refined the grains and increased tensile strength and elongation at ambient temperature. Banoth et al. [15] processed HX powders with 0.05 wt.% Y additions via LPBF, achieving Y_2O_3 dispersoids in grain interiors and boundaries after solidification. The dispersoids improved creep fracture strain and lifetime at 900 °C, directly through dispersion strengthening and indirectly by reducing oxygen segregation at grain boundaries, which embrittles the alloy.

In this paper, we mechanically-alloy Y_2O_3 nanometric powders into HX powders and process the alloy via LPBF, a method used in other ODS superalloys, e.g., Y_2O_3_ODS-Inconel 718 [16,17], and Y_2O_3_ODS-CM247LC [18,19]. We investigate the grain microstructure and texture, with and without addition of Y_2O_3 dispersoids, and correlate them with the creep properties, measured at 950 °C for two different orientations with respect to the build direction.

* Corresponding author.
E-mail address: jovid.rakhmonov@northwestern.edu (J.U. Rakhmonov).

https://doi.org/10.1016/j.addlet.2022.100069
Received 27 May 2022; Received in revised form 20 June 2022; Accepted 21 June 2022

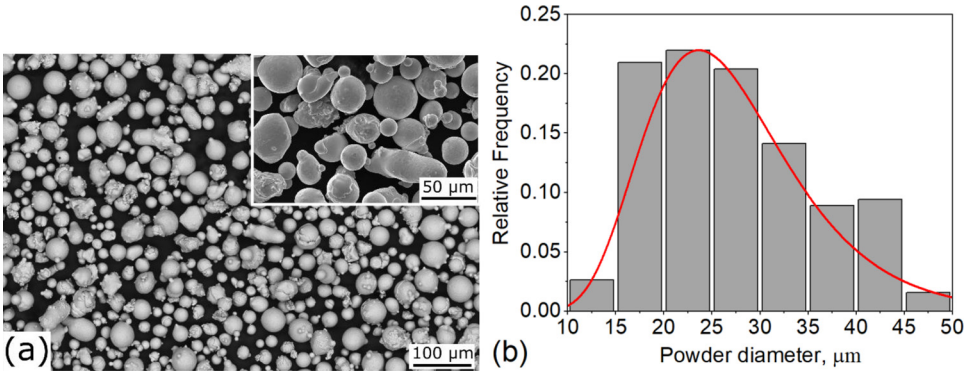

Fig. 1. (a) SEM micrograph showing the morphology and (b) size distribution of the HX alloy powders with the fitted log-normal distribution curve.

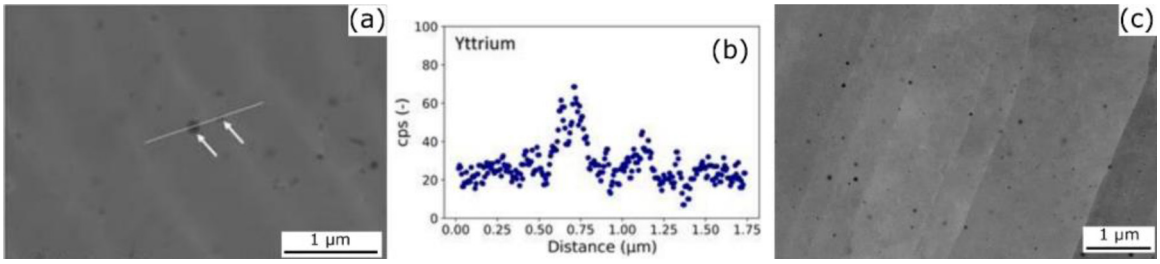

Fig. 2. (a) Backscattered (BSE) SEM micrograph showing distribution of Y-rich oxides (dark particles) and (b) EDS line-scan corresponding to the white line in (a) and showing Y enrichment in these fine, equiaxed precipitates; (c) BSE-SEM micrograph showing the distribution of Y-rich oxides at both grain interiors and boundaries.

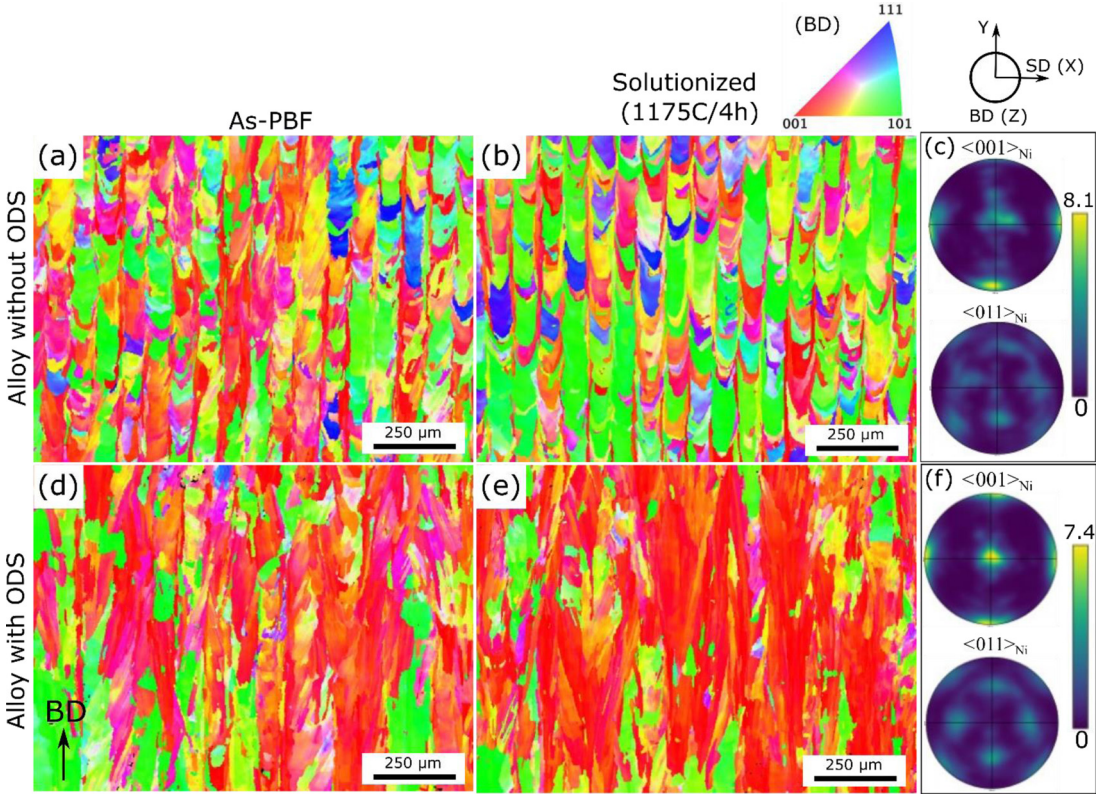

Fig. 3. (a,b,d,e) EBSD inverse pole figure (IPF) maps acquired from as-powder-bed fused (as-PBF) (a,d) and solutionized (b,e) alloys (a,b) without and (d,e) with ODS; (c,f) pole figures representing as-solutionized HX alloys (c) without and (f) with ODS, corresponding to (b) and (e), respectively. BD and SD refer to build and scanning directions, respectively.

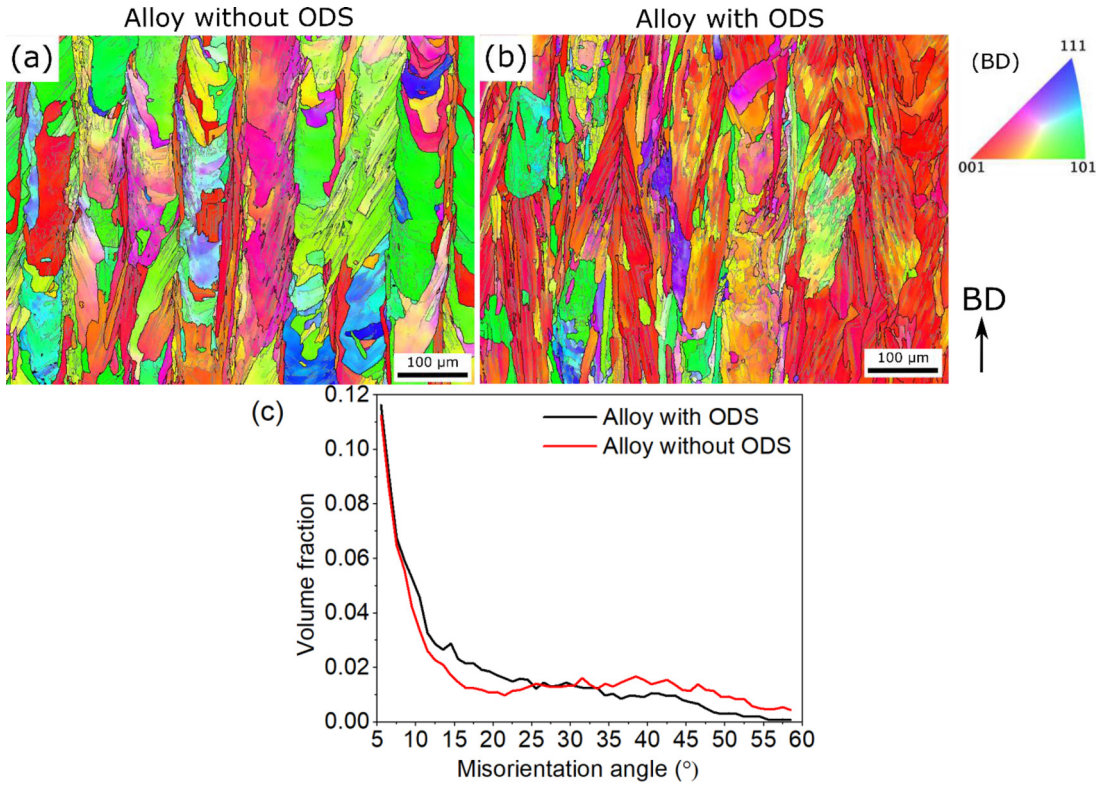

Fig. 4. (a,b) EBSD inverse pole figure (IPF) maps acquired from as-powder-bed fused (as-PBF) HX alloy (a) without and (b) with ODS. Black and gray lines indicate high-angle ($\varphi \geq 15^{\circ}$) and low-angle ($15^{\circ} > \varphi \geq 2^{\circ}$) grain boundaries, respectively; (c) distribution of misorientation angle measured for IPF maps in (a,b) using a minimum threshold angle of 5°.

2. Experimental procedures

Inert-gas atomized HX powders (from Oerlikon AM, Germany) were used, with composition measured by inductively-coupled plasma – optical-emission spectrometry (ICP-OES) reported in

The HX powders exhibit a near-spherical morphology often with some small satellite powders attached to the coarser ones (Fig. 1a). Diameter of powders varies between 10 and 50 μm and follows log-normal distribution (Fig. 1b), with a mean value of ~ 27 μm. Nanometric 99.99% pure Y_2O_3 powder (10 nm average particle size, from US Research Nanomaterials) was blended, at a concentration of 1 wt.%, with the HX powder by ball-milling (ZrO_2 media, ball-to-powder ratio: 5:1) in Nalgene polypropylene containers on a rotational mill for 24 h. The powders remain spheroidal after ball milling.

Two blocks (15×27×14 mm) - one from the unmodified HX powders and the other from the ODS powders - were consolidated on a powder-bed fusion (PBF) machine, (Sisma MySint 100, Trumpf), equipped with a 200 W fiber-laser operating in continuous-wave mode with a 55 μm spot size and 1070 nm wavelength. A bidirectional scan strategy (90° rotation between layers) was conducted under Ar shielding gas (O_2 < 0.01%) with a laser power of 150 W, scanning speed of 550 mm/s, hatch spacing of 100 μm and a layer thickness of 30 μm, followed by a contour scan, at 60 W power, 300 mm/s scanning speed.

The consolidated blocks were separated from the stainless steel base-plate by electro-discharge machining (EDM). Cylindrical compressive creep specimens (diameter: 5 mm, height: 11 mm) were then machined from the blocks by EDM in the vertical (build direction z parallel to the load direction) and horizontal direction (scan direction x parallel to the loading direction), yielding 4 cylinders per direction from a single block. The remaining material was used for microstructural analysis.

Prior to creep tests, creep specimens were solutionized in air at 1175 °C for 4 h and then preconditioned (aged) at 950 °C for 120 h. This heat-treatment avoids the formation of σ−phase, while small amounts of μ-phase are still present. Upon completion of each heat treatment, the specimens were quenched in water at room temperature. Compressive creep tests were performed in air at 950 (±3) °C (as measured with a K-type thermocouples attached to the specimen, using the stress-jump method). For each applied stress level, strain was measured using a linear variable differential transducer (LVDT) until a steady-state strain rate was achieved. Thereafter, the stress is increased to a higher value and the procedure is repeated until ~10% plastic strain accumulated in the specimen. At least two specimens per alloy condition were tested to assess repeatability.

Microstructures of the alloys before and after creep were studied using scanning electron microscopy (SEM, FEI Quanta 650), equipped with electron backscatter diffraction (EBSD). Specimens for microstructure analyses were prepared by employing standard mounting, grinding, and polishing techniques.

3. Results and discussion

3.1. Microstructure

As-processed density was 8.30 g/cm^3 measured by the Archimedes method, indicating near-full densification, which was confirmed by SEM observations of cross-section revealing very rare pores and no cracks. Fig. 2a shows the distribution of fine, equiaxed precipitates (dark ones) throughout the microstructure and the EDS line-scan (Fig. 2b) that corresponds to the line drawn in Fig. 2a, reveals Y enrichment in these precipitates, which are expected to be Y_2O_3 dispersoids In general, Y-rich oxide dispersoids are found distributed at both interiors and boundaries of the grain (Fig. 2c). Previous study on LPBF of blended powders composed by Y_2O_3 and pre-alloyed Ni-Cr-Al-Ti has shown that Y_2O_3

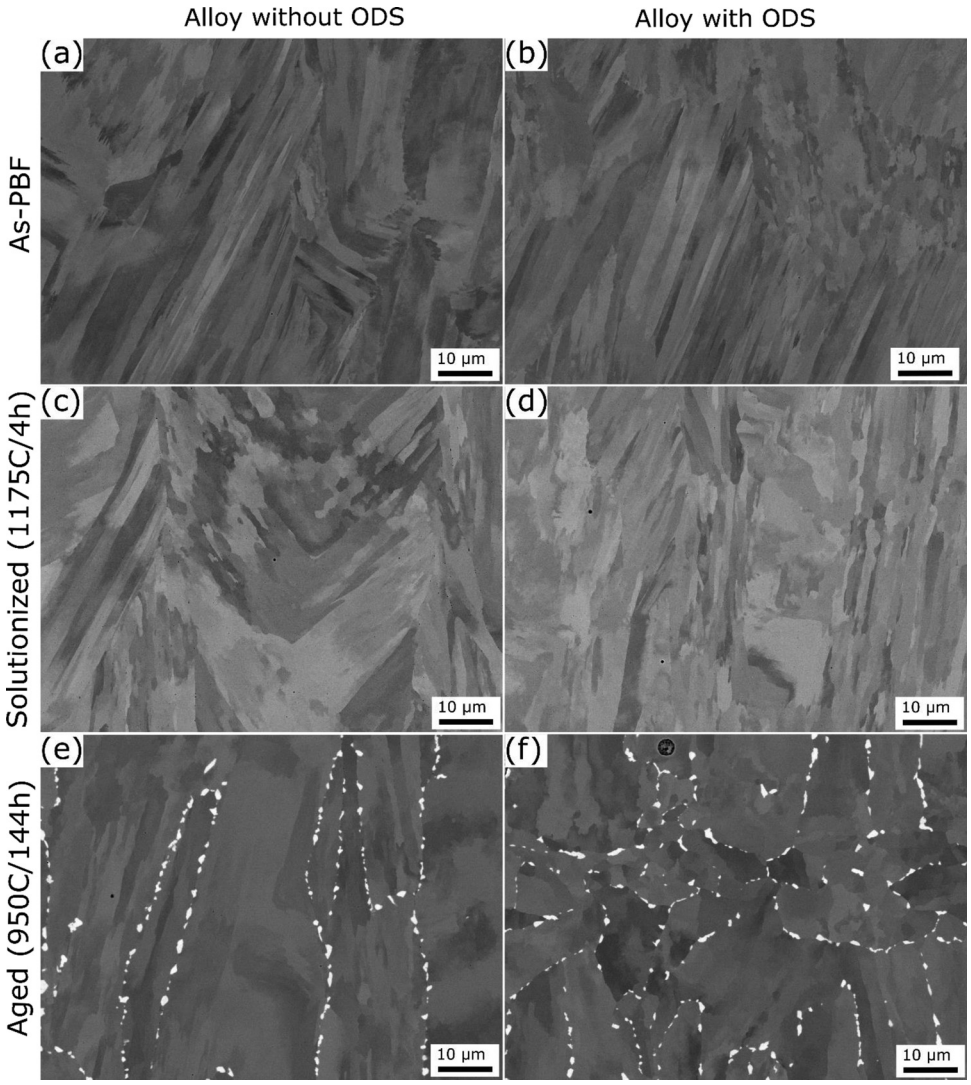

Fig. 5. (a-f) SEM backscattered electron micrographs showing the microstructure of the non-ODS (a,c,e) and ODS (b,d,f) HX alloys in as-PBF (a,b), solutionized (c,d) and aged (e,f) conditions. Build direction is vertical for (a-e) and perpendicular to image plane for (f).

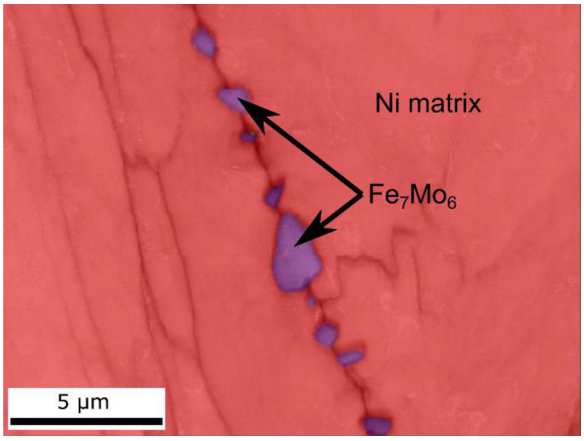

Fig. 6. EBSD phase-contrast map showing μ-Fe_7Mo_6 precipitates at a grain boundary. The matrix and Fe_7Mo_6 are successfully indexed using Ni and Fe_7W_6 (which is isomorphous to Fe_7Mo_6) phases.

dispersoids remain largely stable to decomposition during printing due to their extreme thermal stability [18].

Fig. 3 shows inverse pole figure (IPF) maps acquired from as-powder-bed fused (as-PBF) and solutionized alloys with and without oxide dispersion strengthening (ODS). Elongated grains are clearly aligned along the build direction for both alloys, with no evidence of recrystallization occuring during printing or solutionizing. In the non-ODS alloy, most of the elongated grains are aligned with either <011> or ⟨001⟩ directions along the build direction (BD) (Fig. 3a,b), as also shown in the corresponding pole figures (Fig. 3c). Strong alignement of the ⟨001⟩ directions with the scanning direction (SD) is also observed (Fig. 3c), indicating absence of a ⟨001⟩ fiber texture (random orientation distribution in directions perpendicular to BD) for our alloy, which is often observed in as-PBF or axisymetrically-deformed (in tension) FCC metals [20,21]. Consistent with our texture, Pistor and Körner [22] have shown in a Ni-based superalloy extreme grain alignment with ⟨001⟩ directions, i.e., [001] and [010] aligned respectively along build direction and melt direction (MD, which is perpendicular to the scanning direction, occuring when melt pools are with persistent line shapes [23]), at the early stages of the building process; however, with increasing build height, the grains experience continuous twisting around the BD-axis until their ⟨011⟩ orientations become fully aligned with the MD [22]. This enables, upon subsequent build height increase, the solidification of a monocrystalline sample with $<001>_{Ni}$//BD and $<011>_{Ni}$//MD orientation [22]. However, no $<011>_{Ni}$//BD grains are observed, and the presence of $<011>_{Ni}$//MD grains is attributed to the thermally-induced

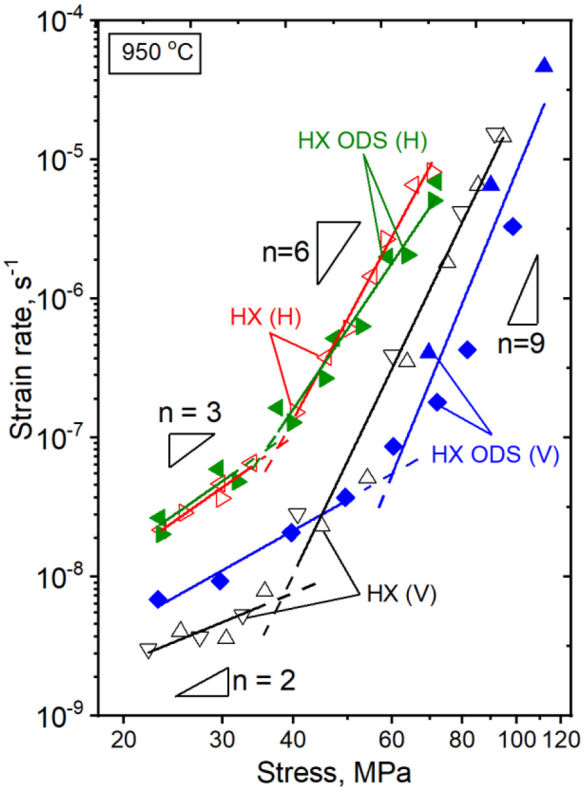

Fig. 7. Double-logarithmic plot of steady-state strain rate vs. compressive stress, for solutionized and aged HX alloys, with and without ODS, loaded vertically (V) and horizontally (H).

stress and strain fields existing near the melt pool, leading to plastic deformation of the solidifying material.

By contrast, our ODS alloy exhibits predominantly $<001>_{Ni}$//BD grains and much fewer $<011>_{Ni}$//BD grains (Fig. 3d,e,f). The $<001>_{Ni}$//BD grains have ⟨001⟩ directions parallel to the scanning direction in the ODS alloy too (Fig. 3f). Surface energy anisotropy in FCC metals promotes grain growth along ⟨001⟩ orientations [24]. The grains with ⟨001⟩ orientations that are aligned with the direction of the thermal gradient overgrow other grains oriented differently with respect to the thermal gradient, resulting in the formation of ⟨001⟩ textures during directional solidification [22,24]. The fact that the grains with ⟨001⟩ orientations in our alloy are also aligned with the SD might imply the presence of strong thermal gradient along both BD and SD. However, *a* $<011>_{Ni}$//BD texture cannot be explained by the theory of grain selection during directional solidification of FCC metals [22,24]. FCC metals, under compressive deformation, produces ⟨011⟩ deformation texture along the loading direction. For example, Um et al. showed the evolution of ⟨011⟩ fiber texture during ambient-temperature compressive deformation of a 99.9% Ni rod with initial ⟨111⟩ + ⟨001⟩ fiber textures created via axisymmetric extrusion [25]. Pistor and Körner [22] have attributed the evolution of $<011>_{Ni}$//MD grains to the thermally-induced stress and strain fields existing in the neighbourhoud of the melt pool, leading to the compressive deformation of the solidifying material along MD. As discussed further, high density of low-angle grain boundaries, i.e., dislocations and subgrain boundaries, are observed at the grain interiors of as-built alloys (Fig. 4), suggesting that grains are plastically deformed during the building process. However, to relate the observed $<011>_{Ni}$//BD grains (Fig. 3) to the thermally-induced stress and strains in the neighbourhoud of the melt pool requires in-depth studies of their distribution via finite-element modeling, which is beyond the scope of this study.

As shown in Figs. 4a,b and 5(a,b), both alloys exhibit low-angle grain boundaries (subgrain boundaries) in the as-printed state, indicative of plastic deformation during printing, with subgrain boundaries forming via dynamic/static recovery, as hypothesized above. The difference in the subgrain structure of the alloys seems insignificant; however, misorientation angle distribution quantified for IPF maps in Fig. 4a,b reveals slightly higher fraction of low-angle grain boundaries at the expense of high-angle grain boundaries in ODS alloy as compared to non-ODS alloy (Fig. 4c). This implies that oxide dispersoids, due to their interaction

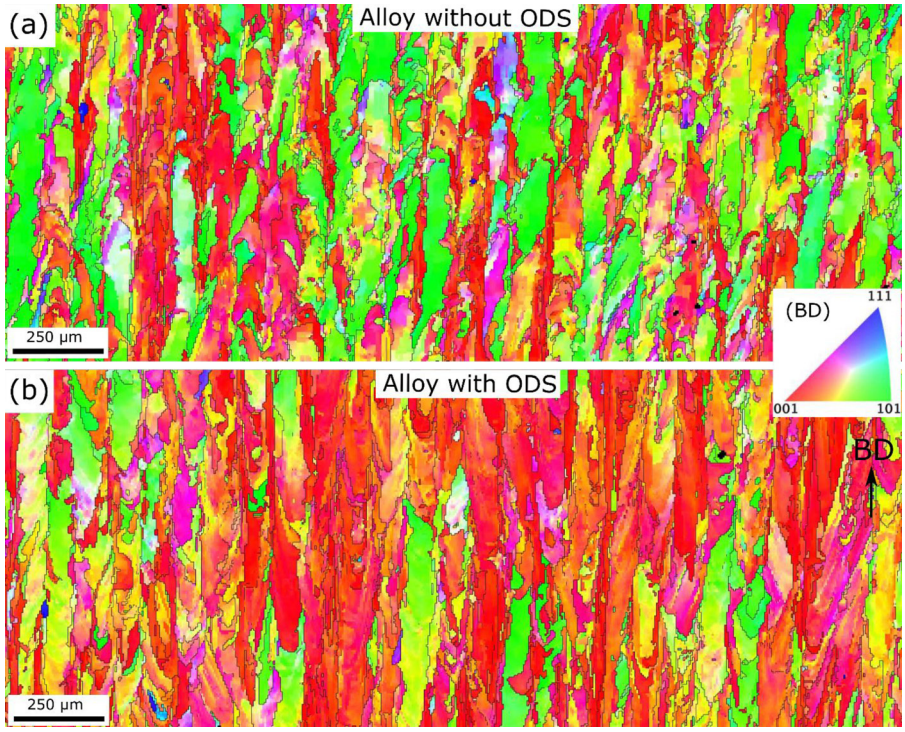

Fig. 8. EBSD IPF maps showing the grain structure and orientations for vertically loaded HX alloys (a) without and (b) with ODS, crept at 950 °C. Build direction is vertical.

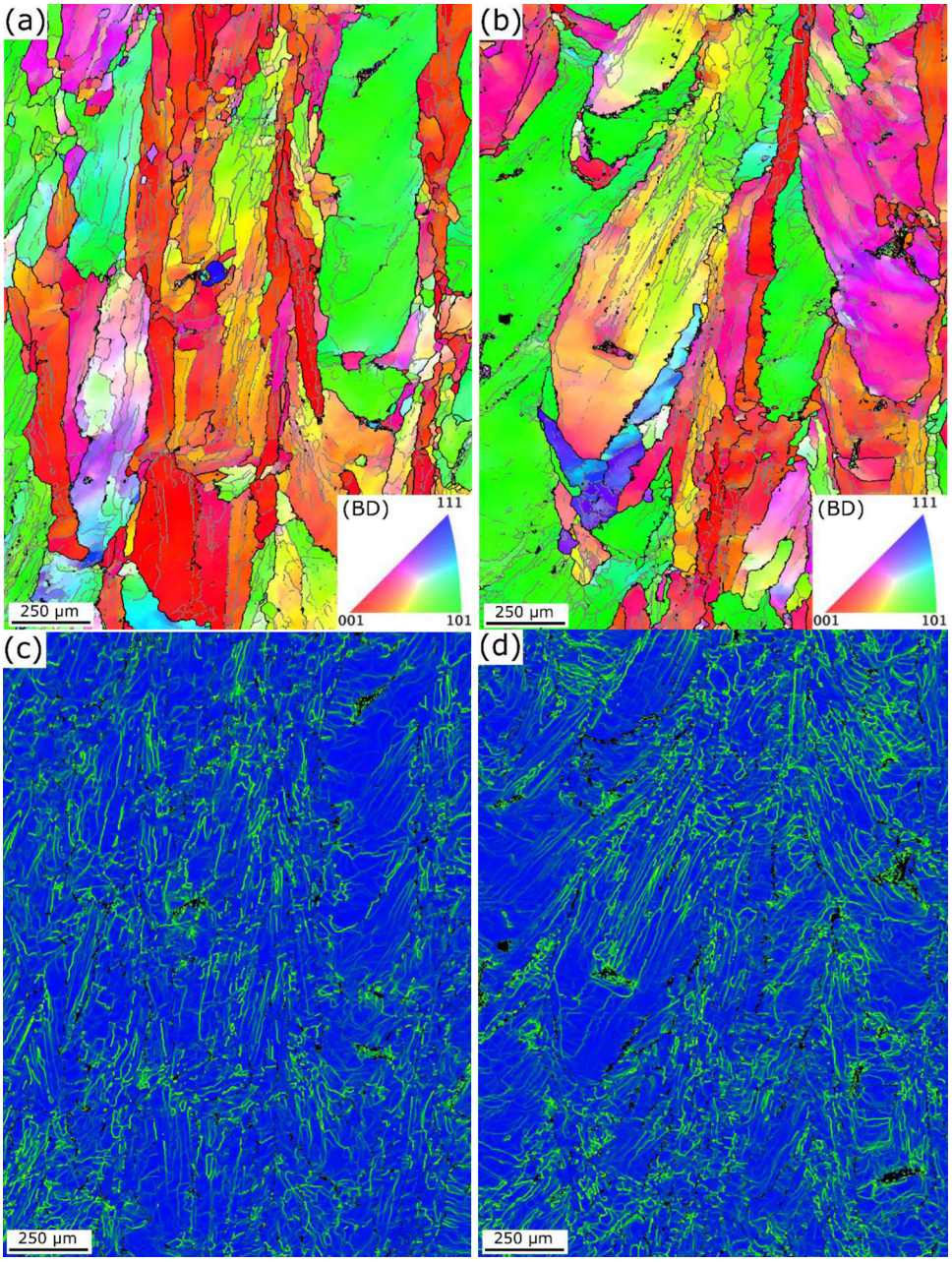

Fig. 9. (a,b) EBSD IPF and (c,d) kernel average misorientation (KAM) maps showing the sub-grain structure and orientations for vertically loaded HX alloys (a) without and (b) with ODS, crept at 950 °C. Black and gray lines in (a,b) indicate high-angle ($\varphi \geq 15^{\circ}$) and low-angle ($15^{\circ} > \varphi \geq 2^{\circ}$) grain boundaries, respectively. The maximum angle for KAM analyses is set at 5° Build direction is vertical for all maps.

with dislocations, likely influence the rate of recovery which our alloy experiences during printing process.

Figs. 5(a-f) illustrate microstructures of both ODS and non-ODS alloys in their as-PBF, solutionized and aged states. Due to the orientation contrast in the micrographs, the subgrains formed during printing are clearly visible. Solutionizing does not appear to alter the subgrain structure of both alloys (Figs. 5c,d). Due to the relatively fine grain structure of the alloy, their homogenization is expected to occur faster as compared to their cast counterparts. Upon aging of both alloys, however, grain boundaries become decorated by precipitates (Fig. 5e,f). As these precipitates are well indexed via EBSD using the μ-Fe_7W_6 phase (Fig. 6), they are identified as Fe_7Mo_6, which is isomorphous to the Fe_7W_6 phase. These precipitates are observed at high-angle grain boundaries rather than low-angle grain boundaries, consistent with an easier nucleation at the former sites. Precipitation of μ-phase has been reported to occur in binary Fe-W (Fe_7W_6), Fe-Mo (Fe_7Mo_6), Co-Mo (Co_7Mo_6) and Co-W (Co_7W_6) [26]. Given complexity of our alloy, several alloying elements, such as Co, Mn and W, are expected to partially substitute either Fe or Mo in this phase.

3.2. Creep behavior

A typical creep strain curve evolving as function of time and applied stress level at 950 °C for horizontally loaded HX alloy with ODS is exemplarily shown in Fig. S1. The minimum strain rate $\dot{\varepsilon}$ vs. stress σ, measured at 950 °C for both alloys, were plotted in a double-logarithmic manner, as shown in Fig. 7, according to the Norton creep power law:

$$\dot{\varepsilon} = A\,\sigma^{n} \exp\left(-\frac{Q}{RT}\right) \tag{1}$$

where A is a constant, n is the stress exponent, Q is the activation energy, and R and T have their usual meanings.

The anisotropy of the creep response was investigated by tests carried out with uniaxial loading direction parallel or perpendicular with

Table 1
Chemical composition (wt.%) of Hastelloy X powder.

Ni	Cr	Fe	Mo	Co	W	Mn
Bal	21.06	17.80	8.92	2.07	0.74	0.43

the build direction (BD), which are respectively referred to as vertically (V) or horizontally (H) loaded alloys. Vertically-loaded alloys exhibit two creep regimes with distinct stress exponent, n. At lower stresses (up to 40–50 MPa), the stress exponent is low, n ~ 2, consistent with diffusional creep being rate-limiting [27]. At higher stresses, the stress exponent is much higher, n ~ 9, as expected if dislocation climb is rate-limiting. Comparing the two vertically-loaded alloys with and without ODS, the Y_2O_3 dispersoids have a clear influence on creep deformation: (i) at low stresses, the ODS alloy is weaker, showing a doubling in strain rate, at a given stress, as compared to the non-ODS alloy; (ii) at high stresses, the ODS alloy is stronger, displaying a five- to six-fold decrease in strain rate as compared to the non-ODS alloy (Fig. 7). The lower creep resistance of the ODS alloy in the diffusional regime may be due to a slightly smaller grain size, possibly related to grain boundary pinning by the oxide dispersoids preventing grain growth. As grains are highly elongated (Fig. 5), grain-boundary sliding needed to accommodate diffusional creep is more complex than for equiaxed grains, and the presence of Fe_7Mo_6 precipitates at grain boundaries likely restrict grain-boundary sliding. Nevertheless, our results show that the influence of Y_2O_3 dispersoids on the rate of diffusional creep is minor. By contrast, the much higher creep resistance of the ODS alloy in the high-stress region implies that the dispersoids are effective at inhibiting dislocation motion. Eq. (1),Table 1

Horizontally-loaded alloys display the same two creep regimes and similar stress exponents (n ~ 3 and n ~ 6, above and below ~ 35 MPa, respectively). As compared to their vertically-loaded counterparts, horizontally-loaded specimens show much lower creep resistance, with almost one order of magnitude difference in strain rate, at a given stress. This strong anisotropy in creep response is consistent with the high level of grain texture. Furthermore, the much faster diffusional creep rate may also be linked to the highly anisotropic grain shape of the alloys, and the fact that grain boundaries on which Fe_7Mo_6 precipitates are located are highly aligned. Unexpectedly, when tested horizontally, there is no difference between the ODS and non-ODS alloys in both creep regime, which may be because the various differences in microstructure (texture and grain shape) have cancelling effects on the creep rate. However, further studies are still required to reveal the effect of oxide dispersoids on anisotropic creep response of HX alloys.

Figs. 8(a,b) shows EBSD-IPF maps, along the build direction, for vertically-loaded crept samples, without and with ODS, after ~ 10% compressive strain. Grains remain aligned along the build direction for both alloys, with no evidence of dynamic recrystallization having occured during creep deformation. Similar to the as-printed states, grains with $<001>_{Ni}$//BD and $<011>_{Ni}$//BD are widespread in the non-ODS alloy, whereas grains with $<001>_{Ni}$//BD provide the dominant texture component in the ODS alloy after creep deformation. This indicates that the grain microstructure remains largely unchanged after creep despite high level of internal energy stored in these alloys in the form of sub-grain boundaries formed on printing (Fig. 4). However, it is possible that both alloys experienced dynamic recovery during creep to a certain extent, as evidenced by the much reduced low-angle grain boundaries within the grains of the crept alloys (Fig. 9a,b) as compared to those in the as-printed alloys (Fig. 4a,b). The high levels of primary creep observed for these alloys, particularly at the first applied stress during the stress-jump creep experiment, is consistent with our hypothesis of dynamic recovery, until a steady-state sub-grain structure is established at the initial stress during creep. The kernel average misorientation (KAM) maps in Fig. 9(c,d) show misorientation concentrated heterogeneously within grain interiors. No apparent difference is seen between ODS and non-ODS alloys.

4. Conclusions

Hastelloy-X alloy powders, with and without addition of 1 wt.% Y_2O_3 nanometric powders, were consolidated via laser powder-bed fusion. The main conclusions are:

1 Specimens, with and without oxide additions, are nearly full densified and crack-free, and they show elongated grains aligned in the build direction with a pronounced texture given by a strong alignment of ⟨001⟩ family of orientations along both build and laser scanning directions.
2 Creep tests performed at 950 ˚C with the uniaxial compressive stress parallel to the build direction (i.e., aligned with the elongated, textured grains) reveal two creep regimes:
   a diffusional creep at low stresses (below 50 MPa), where the ODS alloy is less creep resistant than the oxide-free alloy, consistent with a smaller grain size resulting from grain-boundary pinning by the oxide dispersoids;
   b dislocation creep at high stresses (from 50 to 120 MPa), where the ODS alloy is more creep resistant (with a ~5-fold decrease in strain rate for a given stress), than the oxide-free alloy, as expected from oxide dispersoids impeding dislocation motion.
3 When the compressive creep stress is applied perpendicular to the aligned, textured grains, both alloys creep much faster than in the parallel direction, but the effect of oxide dispersoids is negligible, reflecting a complex interplay between texture, grain shape, grain size, and μ-Fe_7Mo_6 grain-boundary precipitates.
4 After ~10% compressive creep deformation, grain structure and texture remain largely unchanged, indicating a strong resistance against dynamic recrystallization.

Declaration of Competing Interest

Prof. David Dunand discloses a financial interest in NanoAl, LLC which is part of Unity Aluminum, companies which are active in the field of cast and additively-manufactured aluminum alloys.

Acknowledgments

This research was funded by the US Army Research Office (W911NF-18–1–0129). It made use of the MatCI Facility and the NUANCE Center at Northwestern University, which received support from the MRSEC program (NSF DMR-1720139) at the Materials Research Center and the SHyNE Resource (NSF ECCS-1542205). JUR acknowledges the financial support from the US Army Research Laboratory through award W911NF-19–2–0092.

Supplementary materials

Supplementary material associated with this article can be found, in the online version, at doi:10.1016/j.addlet.2022.100069.

References

[1] A. Ghasemi, A.M. Kolagar, M. Pouranvari, Microstructure-performance relationships in gas tungsten arc welded Hastelloy X nickel-based superalloy, Mater. Sci. Eng. 793 (2020) 139861.
[2] C. Capdevila, H.K.D.H. Bhadeshia, Manufacturing and Microstructural Evolution of Mechanuically Alloyed Oxide Dispersion Strengthened Superalloys, Adv. Eng. Mater. 3 (9) (2001) 647–656.
[3] T. Zhang, Z. Xie, J. Yang, T. Hao, C. Liu, The thermal stability of dispersion-strengthened tungsten as plasma-facing materials: a short review, Tungsten 1 (3) (2019) 187–197.
[4] S.-.H. Jeong, S.-.H. Kang, C.-.H. Han, T.-.K. Kim, D.-.H. Kim, J.-.S. Jang, Microstructural Evaluation and High Temperature Mechanical Properties of Ni-22Cr-18Fe-9Mo ODS Alloy, J. Korean Powder Metal. Inst. (2011).

[5] M. Hasegawa, M. Osawa, Oxide dispersion strengthened nickel-base heat resistant alloys by means of the spray-dispersion method, Metall. Trans. A 16 (6) (1985) 1043–1048.
[6] A.N. Jinoop, C.P. Paul, S.K. Nayak, J.G. Kumar, K.S. Bindra, Effect of laser energy per unit powder feed on Hastelloy-X walls built by laser directed energy deposition based additive manufacturing, Opt. Laser Technol. 138 (2021) 106845.
[7] M. Dinovitzer, X. Chen, J. Laliberte, X. Huang, H. Frei, Effect of wire and arc additive manufacturing (WAAM) process parameters on bead geometry and microstructure, Addit. Manuf. 26 (2019) 138–146.
[8] Q. Han, Y. Gu, S. Soe, F. Lacan, R. Setchi, Effect of hot cracking on the mechanical properties of Hastelloy X superalloy fabricated by laser powder bed fusion additive manufacturing, Opt. Laser Technol. 124 (2020) 105984.
[9] B. Guo, Y. Zhang, Z. Yang, D. Cui, F. He, J. Li, Z. Wang, X. Lin, J. Wang, Cracking mechanism of Hastelloy X superalloy during directed energy deposition additive manufacturing, Addit. Manuf. 55 (2022) 102792.
[10] Q. Han, R. Mertens, M.L. Montero-Sistiaga, S. Yang, R. Setchi, K. Vanmeensel, B. Van Hooreweder, S.L. Evans, H. Fan, Laser powder bed fusion of Hastelloy X: effects of hot isostatic pressing and the hot cracking mechanism, Mater. Sci. Eng. 732 (2018) 228–239.
[11] D. Tomus, P.A. Rometsch, M. Heilmaier, X. Wu, Effect of minor alloying elements on crack-formation characteristics of Hastelloy-X manufactured by selective laser melting, Addit. Manuf. 16 (2017) 65–72.
[12] R. Ghiaasiaan, M. Muhammad, P.R. Gradl, S. Shao, N. Shamsaei, Superior tensile properties of Hastelloy X enabled by additive manufacturing, Mater. Res. Lett. 9 (7) (2021) 308–314.
[13] A.N. Jinoop, V. Anil Kumar, C.P. Paul, R. Ranjan, K.S. Bindra, Hot deformation behavior of Hastelloy-X preforms built using directed energy deposition based laser additive manufacturing, Mater. Lett. 270 (2020) 127737.
[14] X. Cheng, Y. Zhao, Z. Qian, J. Wu, J. Dong, Z. Ma, Y. Liu, Crack elimination and mechanical properties enhancement in additive manufactured Hastelloy X via in-situ chemical doping of Y2O3, Mater. Sci. Eng. 824 (2021) 141867.
[15] S. Banoth, T.N. Palleda, T. Saito, H. Murakami, K. Kakehi, Effects of yttrium and silicon contents in Hastelloy-X built by selective laser melting process, J. Alloys Compd. 896 (2022) 163050.
[16] M. Yesim Yalcin, C. Bora Derin, E. Aydogan, Development and Additive Manufacturing of Oxide Dispersion Strengthened Inconel 718: thermochemical and Experimental Studies, J. Alloys Compd. (2022) 165193.
[17] Q.-ss. Song, Y. Zhang, Y.-ff. Wei, X.-yy. Zhou, Y.-ff. Shen, Y.-mm. Zhou, X.-mm. Feng, Microstructure and mechanical performance of ODS superalloys manufactured by selective laser melting, Opt. Laser Technol. 144 (2021) 107423.
[18] C. Kenel, A. De Luca, S.S. Joglekar, C. Leinenbach, D.C. Dunand, Evolution of Y2O3 dispersoids during laser powder bed fusion of oxide dispersion strengthened Ni-Cr-Al-Ti γ/γ' superalloy, Addit. Manuf. 47 (2021) 102224.
[19] A. De Luca, C. Kenel, S. Griffiths, S.S. Joglekar, C. Leinenbach, D.C. Dunand, Microstructure and defects in a Ni-Cr-Al-Ti γ/γ' model superalloy processed by laser powder bed fusion, Mater Des. 201 (2021) 109531.
[20] J. Rakhmonov, K. Liu, P. Rometsch, N. Parson, X.G. Chen, Effects of Al(MnFe)Si dispersoids with different sizes and number densities on microstructure and ambient/elevated-temperature mechanical properties of extruded Al-Mg-Si AA6082 alloys with varying Mn content, J. Alloys Compd. (2020) 157937.
[21] J. Wu, X.Q. Wang, W. Wang, M.M. Attallah, M.H. Loretto, Microstructure and strength of selectively laser melted AlSi10Mg, Acta Mater. 117 (2016) 311–320.
[22] J. Pistor, C. Körner, A novel mechanism to generate metallic single crystals, Sci. Rep.-Uk 11 (1) (2021) 24482.
[23] J. Pistor, C. Breuning, C. Körner, A Single Crystal Process Window for Electron Beam Powder Bed Fusion Additive Manufacturing of a CMSX-4 Type Ni-Based Superalloy, Materials (Basel) 14 (14) (2021) 3785.
[24] A. Plotkowski, J. Ferguson, B. Stump, W. Halsey, V. Paquit, C. Joslin, S.S. Babu, A. Marquez Rossy, M.M. Kirka, R.R. Dehoff, A stochastic scan strategy for grain structure control in complex geometries using electron beam powder bed fusion, Addit. Manuf. 46 (2021) 102092.
[25] K.K. Um, H.T. Jeong, S.B. Lee, D.N. Lee, Analysis of Compression Textures of Aluminum and Nickel Rods, Mater. Sci. Forum 408-412 (2002) 595–600.
[26] C.C. Silva, C.R.M. Afonso, A.J. Ramirez, M.F. Motta, H.C. Miranda, J.P. Farias, Assessment of microstructure of alloy Inconel 686 dissimilar weld claddings, J. Alloys Compd. 684 (2016) 628–642.
[27] O.D. Sherby, E.M. Taleff, Influence of grain size, solute atoms and second-phase particles on creep behavior of polycrystalline solids, Mater. Sci. Eng. 322 (1) (2002) 89–99.